



HAL
open science

Micro-structuration of a sol-gel architecture for channel waveguide / diffraction grating coupling

M. Bonnel, D. Riassetto, Alain Morand, D. Bucci, M. Langlet

► To cite this version:

M. Bonnel, D. Riassetto, Alain Morand, D. Bucci, M. Langlet. Micro-structuration of a sol-gel architecture for channel waveguide / diffraction grating coupling. *Optical Materials*, 2019, 92, pp.36-45. 10.1016/j.optmat.2019.04.009 . hal-02099741

HAL Id: hal-02099741

<https://hal.univ-grenoble-alpes.fr/hal-02099741>

Submitted on 22 Oct 2021

HAL is a multi-disciplinary open access archive for the deposit and dissemination of scientific research documents, whether they are published or not. The documents may come from teaching and research institutions in France or abroad, or from public or private research centers.

L'archive ouverte pluridisciplinaire **HAL**, est destinée au dépôt et à la diffusion de documents scientifiques de niveau recherche, publiés ou non, émanant des établissements d'enseignement et de recherche français ou étrangers, des laboratoires publics ou privés.



Distributed under a Creative Commons Attribution - NonCommercial 4.0 International License

Micro-structuration of a sol-gel architecture for channel waveguide / diffraction grating coupling

M.Bonnel¹, D.Riassetto¹, A.Morand², D.Bucci², M.Langlet^{1*}

¹*Univ. Grenoble Alpes, CNRS, Grenoble INP, LMGP, F-38000 Grenoble, France*

²*Univ. Grenoble Alpes, CNRS, Grenoble INP, IMEP-LAHC, F-38000 Grenoble, France*

* michel.langlet@grenoble-inp.fr

Abstract: A flagship application of miniaturized chemical optical (CO) sensors is the real-time monitoring of cell cultures in the biomedical field. Most of these devices are based on fluorescence variations when a fluorophore encapsulated in the sensor is brought into contact with an analyte. In this context, micro-structured architectures involving light coupling between a channel waveguide and diffraction gratings appear a promising way to propose integrated devices with enhanced detection sensitivity. In this paper, we report for the first time on such micro-structured architecture entirely elaborated through a sol-gel route. This work particularly highlights the potential of a high refractive index titanium oxide based sol-gel photoresist that can be imprinted through a single photolithography step (selective insolation / development) to form a given pattern, thus avoiding multi-step and rather costly traditional lithographic procedures. We firstly present a simplified two-step process taking advantage of this photoresist and leading to micro-structured architectures composed of diffraction gratings imprinted on channel waveguides. Both components of these architectures have been optimized on the basis of opto-geometrical characterizations and modeling. Then channel waveguide / diffraction grating coupling assessments are presented and discussed, showing that light coupling can effectively be achieved in the sol-gel architectures. This work constitutes a first step that opens the route to new CO sensors in channel waveguide configuration.

Keywords: Sol-gel process, photolithography, channel waveguide, diffraction grating, chemical optical sensor

1. Introduction

Integrated chemical optical (CO) sensors have attracted tremendous interest over the two past decades for biomedical applications. These sensors enable the control and monitoring of cell cultivation through the real-time measurement of physical-chemical parameters, for instance dissolved oxygen (DO) or pH that are key parameters in the growth and development of biological cells (see a review in [1]). In most cases, CO sensors are based on fluorescence variations when a suitable fluorophore is put in contact with a specific analyte. For instance, in the presence of oxygen, the fluorescence emission of ruthenium(II) diimine complexes and platinum(II) or palladium(II) porphyrins is selectively quenched [1,2]. Thus, the emission intensity or the excited state lifetime decreases with increasing molecular oxygen concentration. The fluorophores are generally entrapped in a thin film organic polymer or a sol-gel host matrix. The sol-gel process involves the hydrolysis and condensation of metal alkoxides to produce a xerogel matrix, i.e. an inorganic network constituted of metal-oxygen chains and alkoxy/hydroxyl chain-end species. Over the ten past years, sol-gel matrices have often been proposed for CO sensor applications since, compared to polymeric matrices, the derived inorganic network leads to better optical transparency and enhanced chemical, thermal, and mechanical stability (see a review in [2]). Many integrated CO sensors are already commercially available, but the research remains intensive in this field [1]. Indeed, while a thin film configuration is ideally suited for integration in miniaturized devices, it suffers limitations in terms of detection limit. For this reason, miniaturized optical components in the form of microfluidic platforms inspired from integrated optics or photonics have recently been the object of tremendous interest in bio-sensing applications (see reviews in [3-5]). Derived miniaturized devices enable the fabrication of portable sensors allowing rapid and sensitive detection of biological parameters.

The most common example of integrated optical component is the planar waveguide, which relies on the well-known principle of light confinement, such as for optical fibers. In planar waveguides, light propagation is achieved through a suitable control of the waveguide core thickness, as well as a suitable mismatch between its refractive index and those of the substrate (or under-cladding layer) and the superstrate (or external medium), where the waveguide core refractive index should be sufficiently high compared to those of the surrounding media. Such a structure allows a vertical confinement of light propagating within the waveguide core. Light confinement in two dimensions can be achieved with a channel waveguide, having a width of finite dimension, which can for instance be obtained by selectively etching a planar waveguide. In this configuration, the optical power field is confined in the width and the thickness of the waveguide core, which favours an enhanced light propagation efficiency. Integrated biosensors based on planar or channel waveguides have been

largely exploited over the last decade [6-13]. In particular, several papers report on such devices elaborated using a sol-gel procedure [14-19]. These papers show that, compared to the numerous techniques traditionally used in the fabrication of integrated optics or photonics devices (e-beam, low pressure CVD, magnetron sputtering, ion exchange...), the sol-gel process provides an ideal trade-off between low cost and easy implementation, optical quality, as well as mechanical and chemical robustness.

The main issue in the exploitation of waveguide-based integrated optical sensors relies on the difficulty to achieve efficient light coupling with the waveguide. Light coupling can be performed by end-fire butting using an optical fiber, but this method is rather demanding in the case of planar or channel waveguides because it necessitates a rigorous end facet polishing of the waveguide and, owing to the weak thickness of this latter (on the order of 0.1 μm), it requires a critical fiber-waveguide alignment tolerance. Light coupling using a prism is a very efficient alternative that does not require critical polishing and alignment, but it can hardly be integrated in a miniaturized device. Thus, several approaches have been considered to relax fiber positioning tolerances and promote efficient end-fire coupling into integrated photonics devices, such as the use of micro-lensed fibers [20] or different variants of taper couplers [21-23]. Another alternative relies on light coupling with diffraction gratings [24]. Such diffracting couplers exhibit relaxed positioning tolerances compared to end-fire butting, they do not require waveguide facet polishing, and they are fully compatible with integration in miniaturized devices. Moreover, these couplers can be easily positioned at both ends of a planar or a channel waveguide in order to favour efficient in- and out-coupling of light. The use of diffracting couplers requires a periodic structure composed of fine patterns whose period should ideally be of the order of the considered wavelength. It is a well-known method in integrated optics and photonics and it has already been exploited in some planar or channel waveguide-based biosensors [3-5]. However, this method has only been the object of punctual studies in this field and its potential has by far not been sufficiently examined. It should also be noted that, to our best knowledge, it has never been exploited using a sol-gel procedure.

Our group is presently involved in the development of a new sol-gel derived micro-structured architecture devoted to the optical sensing of DO. This architecture is based on the fluorescence of tris(4,7-diphenyl-1,10-phenanthroline)ruthenium(II) (Rudpp). Rudpp has extensively been exploited in fluorescence-based sol-gel derived DO sensing devices [2]. It exhibits a large Stokes shift and broad excitation and emission bands located around 460 and 610 nm, respectively. Our ultimate goal in this research is to develop a DO sensitive architecture constituted of a channel waveguide doped with Rudpp and endowed at each extremity with diffracting couplers. In this configuration, the waveguide will propagate the excitation and emission signals, thus implicating a large quantity of fluorophores

that should guaranty an important fluorescence intensity, while the diffraction couplers will provide efficient injection of the excitation signal in the waveguide core and efficient extraction of the emission signal toward a photodetector. This paper reports on a first experimental step toward the final fabrication of a functional DO sensitive architecture. We focus on a simplified architecture with a diffraction grating imprinted on one end of a channel waveguide and we demonstrate for the first time the feasibility of channel waveguide / diffraction grating coupling using a procedure entirely based on the sol-gel process. This work particularly highlights the potential of a high refractive index titanium oxide (TiO₂) based sol-gel photoresist that can be imprinted through a single photolithography step (selective insolation / development) to form a given pattern, thus avoiding multi-step and rather costly traditional lithographic procedures. We show how this photoresist has been extrapolated to a simplified two-step process leading to a micro-structured architecture composed of diffraction gratings imprinted on channel waveguides and how light coupling can effectively be achieved in this architecture.

2. Materials and methods

2.1 Thin films processing

As explained in introduction, an essential criterion for light guiding achievement requires that the waveguide core refractive index is sufficiently higher than that of the substrate, which can be favored by using a low refractive index glass substrate. In this work, we have chosen to investigate a more general procedure that can be adapted to any kind of substrates. Thus, silicon wafers (3 x 3 cm²) were used as model substrates. They were preliminarily heat-treated in air for 2 hr at 500°C to create a thin thermal silica layer at their surface. Hydroxyl groups (-OH) naturally grafted on this silica surface favor the adhesion of a subsequently deposited xerogel film. They were then coated with a low refractive index cladding layer. Beside the necessity of a low refractive index, this latter should be thick enough to suppress any optical interaction between the substrate and the waveguide that would perturb light propagation. For that purpose, we used a sol-gel procedure that has been fully detailed in one of our previous paper [25]. Briefly, a sol was prepared from 2-(3,4-epoxycyclohexylethyltrimethoxysilane) (EETMOS) and tetraethoxysilane (TEOS) diluted in an absolute ethanol/methanol/deionized water/hydrochloric acid mixture. The epoxy function of EETMOS is photo-polymerizable under UVA light, which favors a good chemical stability of derived films deposited at room temperature. Triarylsulfonium hexafluorophosphate (TFP) was used as an initiator of photo-polymerization. The TEOS/EETMOS molar ratio and [EETMOS-TEOS] concentration were fixed at 0.4 and 3.6 M, respectively. The sol was preliminarily heated at 60°C for 38 h and then diluted in absolute ethanol to

fix [EETMOS-TEOS] concentrations ranging from 0.5 to 2.5 M. It was then deposited on the substrate by spin-coating at 3000 rpm. The so-obtained liquid film was dried at room temperature for 5 min, exposed to UVA light (365 nm) for 5 min using a commercial insolation apparatus (UV-KUB from KLOE), and finally post-treated at 110°C for 10 min. This three-step procedure led to a chemically stable xerogel film (named epoxy layer in the following) that sustained a multilayer deposition procedure without any dissolution or deterioration induced by the deposition of a new liquid film. This feature enabled i/ to control the epoxy layer thickness by repeating the single layer deposition steps, and ii/ to support the subsequent deposition of a guiding layer. A high refractive index TiO₂-based guiding layer was then deposited using a sol-gel procedure that has also been fully detailed in another previous paper [26]. In that paper, we showed that derived xerogel films exhibit excellent transparency in the visible range, which is an essential feature for light propagation at the wavelengths considered in the present work (460 and 610 nm). Briefly, a sol was prepared from tetraisopropylorthotitanate (TIPT) and Benzoylacetone (BzAc) diluted in a methanol/butanol/deionized water/hydrochloric acid mixture. The role of BzAc is described hereafter. The BzAc/TIPT molar ratio and TIPT concentration were fixed at 0.6 and 0.5 M, respectively. To deposit guiding layers doped with the fluorophore, a stock solution with a Rudpp concentration of 12.5 mM was prepared in absolute ethanol and various volumes of this solution were added to the Ti-BzAc sol to vary the final Rudpp concentration between 0.2 and 3 mM. So-obtained sols were then deposited by spin-coating at 3000 rpm, subsequently dried at room temperature, and then heat-treated at 110°C for 10 min, leading to doped or not Ti-BzAc xerogel films.

2.2 Photo-patterning procedure

BzAc is a β -diketone which exhibits two C=O double bonds attached to a phenyl ring. The reaction of BzAc with TIPT promotes the opening of these C=O double bonds and a part of the alkoxy groups are readily substituted with β -diketonate ligands to form chelate rings leading to a Ti-BzAc complex. On the one hand, such a complexation reduces the sol-gel reactivity of TIPT, so that Ti-BzAc xerogel films deposited at room temperature and heat-treated at 110°C are chemically unstable and can easily be leached through simple washing with alcohols. On the other hand, BzAc is a photosensitive reagent that undergoes partial photolytic decomposition of the chelate ring when exposed to UVA light. This decomposition leads to alcohol insoluble species (carbonates, carboxylates) that promote the chemical stabilization of the Ti-BzAc xerogel film. These features introduce the principle of the TiO₂-based sol-gel photoresist developed in our group [26]. This one acts as a negative resist where, after selective insolation and appropriate washing, areas exposed to UVA lights remain intact while non-exposed areas are totally removed from the substrate. It can therefore be imprinted through a single photolithography step (selective insolation / development). In the following, the Ti-BzAc resist was

photo-patterned by insolation at 365 nm (UV-KUB from KLOE) in hard contact mode through a chromium mask. This latter was constituted of linear UVA transparent strips and insolation for various durations through strips of various widths was tested. A post-insolation heat-treatment could eventually be performed at 110°C for 8 min to enhance the photo-induced solubility contrasts. After that, the derived patterns were developed in absolute ethanol for a dozen of seconds, rinsed in deionized water to stop the development, and then gently dried with a nitrogen spray. In this work, we have studied a simple two-step deposition / insolation procedure that is summarized in the flow diagram of Fig. 1. More detailed data on this procedure will be provided as part of the 'Results and discussion' section.

2.3 Modeling

Light propagating in a planar or a channel waveguide is described by two polarization modes, i.e. the Transverse Electric (TE) and Transverse Magnetic (TM) modes where the electric and magnetic fields are parallel to the substrate interface, respectively. For instance, if we consider a TE polarization in the simplified case of a planar waveguide, the dispersion relation for guided modes can be written as [27]:

$$\frac{2\pi}{\lambda} d \sqrt{n_c^2 - n_{\text{eff}}^2} - \arctan\left(\sqrt{\frac{n_{\text{eff}}^2 - n_{\text{sub}}^2}{n_c^2 - n_{\text{eff}}^2}}\right) - \arctan\left(\sqrt{\frac{n_{\text{eff}}^2 - n_{\text{sup}}^2}{n_c^2 - n_{\text{eff}}^2}}\right) - m\pi = 0 \quad (1)$$

Where n_c , n_{sub} and n_{sup} are the refractive indices of the waveguide core, the cladding sublayer, and the external medium, respectively, d is the waveguide thickness, and λ the wavelength. This equation can be numerically solved for a certain mode order m and, when such a guided mode exists, it yields the corresponding effective index n_{eff} . Moreover, light confinement in the vertical direction is not perfect and the total reflection at each interface induces an evanescent vertical field profile in surrounding media. For a given guided mode, the extinction coefficient α_{sub} of the evanescent wave in the cladding layer is expressed by [28]:

$$\alpha_{\text{sub}} = \frac{2\pi}{\lambda} \sqrt{n_{\text{eff}}^2 - n_{\text{sub}}^2} \quad (2)$$

The inverse of the extinction coefficient gives the penetration depth in the cladding layer. If the thickness of this latter is superior or equal to 15 times the penetration depth, the interaction between the guided mode and the underneath substrate (here silicon) becomes negligible. In the following, light propagation in our micro-structured architecture has been modelled using the 2D and 3D Mode Solver software developed by Optiwave for the analysis of planar and channel waveguides, respectively. The values of d , n_c and n_{sub} were determined from ellipsometric characterization of Ti-BzAc and epoxy layers. Besides, to provide a first proof of concept of channel waveguide / diffraction grating coupling

in our architecture, we have chosen a simplified configuration where air ($n_{sup} = 1$) has been considered as external medium instead of an aqueous medium ($n_{sup} = 1.33$) that should be further considered in the planned CO sensor application.

As previously explained, this work ultimately aims at developing a micro-structured fluorescent architecture involving a channel waveguide endowed with diffraction gratings at its input and output. The fluorescence excitation signal should be injected in the waveguide by grating-waveguide coupling at the input and the emission signal should be extracted toward a photodetector by waveguide-grating coupling at the output. In this preliminary study, we have chosen to model a simplified architecture involving waveguide-grating coupling, as schematized in Fig. 2. In this configuration, light can be extracted according to a finite number of diffraction angles θ_d by means of a grating coupler of length L having an appropriate period Λ . In order to achieve coupling with a guided mode of effective index n_{eff} , the so-called grating law must be fulfilled [29]:

$$n_{sup} \sin(\theta_d) = n_{eff} + \frac{q\lambda}{\Lambda} \quad (3)$$

Where q is an integer and represents the diffracted coupling orders. If coupling occurs, equation (3) determines a certain number of angles θ_d , where guided light can be radiated toward the external medium. The same equation can be used to describe the reverse configuration where light coupling toward the guided mode occurs from a plane-wave impinging on a grating with an appropriate angle θ_d . In this work, the efficiency of light power radiated toward the external medium has been analyzed for each diffracted order using AFMM (Aperiodic Fourier Modal Method), also known as RCWA (Rigorous Coupled Wave Analysis) modified with PMLs (Perfect Matching Layers). This method has been detailed in previous papers [30,31]. In the following, it has been directly adapted to gratings with an ideal square profile by taking into account their height, width and periodicity. For more complicate profiles, e.g. trapezoidal gratings, a spatial discretization of the slope part (rising and falling edges) was necessary. This part has been defined by the cascade of 10 layers with different core widths and thicknesses.

2.4 Characterization

The fluorescence emission of Rudpp-doped Ti-BzAc layers was measured at room temperature under excitation at 460 nm using a Plate reader infinite 200 PRO – TECAN spectrometer that enables measurements in air or in liquid media. The opto-geometrical properties of epoxy and Ti-BzAc layers, namely the thickness and refractive indices at the Rudpp excitation (460 nm) and emission wavelength (610 nm), were deduced from spectroscopic ellipsometry measurements performed with an AutoSE

HORIBA Scientific device. To extract the thickness and refractive index values, spectral data acquired in the 400-800 nm wavelength range were fitted with the empirical Cauchy model that is commonly employed for transparent materials. The profile and dimensions of photo-imprinted Ti-BzAc patterns were studied by Atomic Force Microscopy (AFM) using a Bruker Dimension Icon device in tapping mode and by stylus profilometry using a Bruker Dektak device. Both methods are complementary since the former provides precise analysis on selected patterns at the micrometer scale while the latter enables to study large patterns on a scale of several tens or hundreds of micrometers. Optical microscopy, using a Leica apparatus, and profilometry were also employed to assess the overall pattern uniformity. Channel waveguide / diffraction grating coupling was tested on simplified architectures using a modal profile measurement bench that enables to measure the 2D intensity profile radiated at the output of the waveguide. Channel waveguides of various widths were endowed at their input with a diffraction grating. Light emerging from a 4 μm diameter optical fiber was injected in the waveguide core via the grating using a devoted set-up allowing XYZ and angular positioning of the fiber. The waveguide output facet was carefully cut and polished using a circular precision saw (DISCO DAD32). Thanks to this polished facet, the emerging light was focused on a Solinocam H2D2 camera through an Mitutoyo objective lens. So-obtained images were first acquired through a Firewire card analyzed with the LabVIEW software. The emerging light intensity converted in a text file was then integrated on the whole waveguide section using the MATLAB software. More detailed data on these measurements are provided in the 'Results and discussion' section.

3. Results and discussion

3.1 Characterization of epoxy and Ti-BzAc layers

- *Fluorescence measurements*

Fig. 3 depicts the fluorescence emission at 610 nm, measured in air and in water under excitation at 460 nm, for Ti-BzAc layers doped with various amounts of Rudpp. The layers were pre-treated at 110°C for 10 min, insolated (without mask) for 40 min and post-treated at 110°C for 8 min. Typical emission spectra are illustrated in the inset of Fig. 3. These spectra exhibit a large maximum between 610 and 650 nm. It suggests that, compared to the pure fluorophore whose fluorescence emission is centered around 610 nm in aqueous solution, the Ti-BzAc environment promotes a slight red-shift and broadening of the Rudpp emission band. Such features have already been reported in various kinds of matrices and are attributed to interactions with the local environment surrounding the fluorophore [32-34]. The emission intensity at 610 nm is observed to increase when increasing the Rudpp concentration up to 2 mM, after what it tends to saturate with further concentration increase. This

saturation is attributed to parasitic phenomena occurring when the concentration of fluorophore in the host matrix exceeds a certain threshold, e.g. concentration quenching or inner filter effects [35].

The main feature depicted in Fig. 3 and its inset is that the fluorescence intensity is much weaker when measured in air compared to that measured in water. It provides an illustration of the quenching effect of oxygen on the Rudpp fluorescence since the concentration of oxygen in air (~275 ppm at room temperature) is around thirty times larger than that in water (~9 ppm at room temperature). In the literature, sol-gel derived thin films [2] or waveguide platforms [15] intended to DO sensing are usually studied using silica-based inorganic or hybrid organic/inorganic matrices. Actually, we could find only one work dealing with sol-gel derived DO sensors using a TiO₂-based xerogel matrix [34]. In that paper, the authors focused on thin film sensors and did not report on the exploitation of planar or channel waveguides. Thus, trends illustrated in Fig. 3 are of particular relevance for our work since they indicate that our original photosensitive Ti-BzAc matrix is compatible with DO sensing, i.e. it does not screen interactions between Rudpp and ambient oxygen and does not disrupt the fluorescence emission of Rudpp and its response to oxygen.

- *Ellipsometric measurements*

The opto-geometrical properties of epoxy layers deposited from sols of various [EETMOS-TEOS] concentrations and/or by using a multi-layer deposition procedure are depicted in Fig. 4. This figure (left) shows that the film thickness gradually increases when increasing the [EETMOS-TEOS] concentration and the number of single layers. Thus, the epoxy layer thickness can be flexibly monitored from a few hundred of nanometers to several micrometers. In the whole range of thicknesses tested here, the uncertainty was inferior to +/- 7%, which accounts both for the thickness uniformity on a same 3x3 cm² sample and to thickness variations between different samples. The refractive indices at 460 and 610 nm of the epoxy layer were observed to slightly increase with its thickness. It is illustrated in Fig. 4 (right) as a function of the number of single layers, and increasing the [EETMOS-TEOS] concentration led to a similar trend. As, for a same composition, the refractive index increases with the material density, these features suggest that increasing the [EETMOS-TEOS] concentration or the number of single layers promotes a slight densification, i.e. a slight volume porosity decrease, in the resulting epoxy layer. Fig. 4 (right) also shows that the refractive index at 460 nm is only slightly superior to that measured at 610 nm, which illustrates that a material of EETMOS-TEOS composition is characterized by a rather flat index dispersion curve. Globally, refractive indices at 460 and 610 nm varied between 1.51 and 1.57 depending on the epoxy layer thickness, and the uncertainty on these values laid in a +/- 0.02 range, which accounts for the sample uniformity and reproducibility. Fig. 5 depicts the opto-geometrical properties of Rudpp-doped Ti-BzAc layers. In that case, only single layers were considered since a multilayer deposition procedure requires a chemical

stabilization of each deposited single layer before deposition of a new one, and this stabilization is not compatible with the photo-imprinting principle of our Ti-BzAc resist. The layers were pre-treated at 110°C for 10 min, insolated (without mask) for 40 min and post-treated at 110°C for 8 min. The absence of post-treatment or some variations in the insolation duration from 10 to 40 min did not produce any significant changes in the opto-geometrical properties. Fig. 5 shows that the layer thickness decreases from 260 to 190 nm when increasing the Rudpp concentration in solution from 0 to 3 mM. It is due to our experimental procedure, where increasing the Rudpp content in the layer requires the addition of an increased volume of the Rudpp stock solution in the Ti-BzAc sol, thus involving a decrease in the titanium alkoxide concentration in the resulting sol. In the whole range of conditions tested here, the thickness uncertainty was inferior to +/- 6%, which accounts here again to the uniformity on 3x3 cm² samples and to the reproducibility between different samples. Besides, the refractive indices of the Ti-BzAc layers appear to be much higher when measured at 460 nm compared to those measured at 610 nm. It illustrates a rather marked index dispersion curve of the Ti-BzAc matrix. The refractive indices are also observed to slightly increase with the content of Rudpp, which is partly attributed to the high atomic mass of ruthenium that tends to increase the density of Rudpp-doped layers. Globally, refractive index values of 1.84 – 1.86 and 1.77 – 1.81 were measured at the 460 and 610 nm wavelengths, respectively, and the uncertainty on these values laid in a +/- 0.01 range. In any cases, these values are thus much higher than those measured for the epoxy layer, which provides a first evidence that a Ti-BzAc/epoxy architecture is compatible with light guiding criteria.

3.2 Photo-patterning of Ti-BzAc layers

Fig. 6 illustrates some examples of Ti-BzAc patterns photo-imprinted on the top of an epoxy layer by insolation through a chromium mask. Only layers non-doped with Rudpp are shown here since we have observed that Rudpp doping does not modify the photo-patterning process. Patterns of widths ranging from 1 to 50 μm were studied and, for the finest ones, we also investigated periodic patterns with widths / pitches ranging from 1 μm / 2 μm to 4 μm / 8 μm. Owing to diffraction limits, widths/pitches of 1 μm / 2 μm constitute the minimal size accessible in this work by insolation through a mask. It is not intrinsically related to our Ti-BzAc resist since we have previously shown that this resist is compatible with submicron diffraction gratings using alternative, but more complex, lithographic methods such as interferometric lithography through a phase mask or microsphere photolithography [36, 37]. In the following, the patterns were photo-imprinted by insolation for 10 to 40 min, followed or not by a post-treatment at 110°C for 8 min. It constitutes the first step of our two-step deposition / insolation procedure (Fig. 1a). Patterns of similar quality could be photo-imprinted regardless of the insolation duration. However, a short insolation of 10 min required a post-treatment to favour

sufficient photo-induced solubility contrasts leading to an efficient post-insolation development. Conversely, increasing the insolation duration up to 40 min yielded enhanced contrasts that did not necessitate any post-treatment. Besides, insolation for 10 min followed by a post-treatment at 110°C did not yield patterns with a chemical stability sufficient to sustain the subsequent deposition of a Ti-BzAc layer, as planned in the second step of our experimental procedure (Fig. 1b). In contrast, the chemical stability obtained after insolation for 40 min was compatible with such a second step, even without post-treatment. Apart from these features, Fig. 6 shows that patterns of similar quality could be obtained regardless of their width. AFM images of this figure depict smooth and regular patterns that nearly respect the width and/or periodicity of the mask strips (Fig. 6a and b). However, a close analysis of these images shows that the patterns do not present vertical edges but rather exhibit a trapezoidal profile with edge slopes around 45°. This feature is attributed to diffraction effects on the edges of the transparent strips during insolation through the mask [26]. Besides, AFM images (Fig. 6a and b) and profilometry data (Fig. 6c and d) depict a good reproducibility and uniformity of the profiles. However, the pattern height of 200-220 nm appears to be weaker, by about 20%, than the thickness of initial (non-doped) Ti-BzAc layers (260 nm). It suggests either that the patterns are partially leached at their top during the post-insolation development or that they are not developed on the whole thickness of the initial layer. Finally, optical microscopic images confirm the overall uniformity of Ti-BzAc patterns (Fig. 6e and f). Such uniform patterns could be obtained on a scale of at least 1 cm, as illustrated in the inset of Fig. 6f by homogeneous diffraction effects for patterns of 1 μm / 2 μm width / pitch.

3.3 Modeling results

Previously exposed opto-geometrical properties of Ti-BzAc layers and derived patterns were used to provide entries for optical modeling. In the following, modeling results, as well as conclusions drawn for further experimentations, are summarized in relation to the expected function of both components constituting the finally planned architecture.

- *Channel waveguides*

An epoxy layer supported waveguide, with an ideally square profile (instead of a true trapezoidal one) and a width of 2 μm , was chosen for modeling at the 460 and 610 nm wavelengths. At each wavelength, for the epoxy layer we considered the whole range of refractive indices depicted in Fig. 4 (right) and, for the Ti-BzAc layer, we considered extremal values of thicknesses and refractive indices corresponding to a 0 mM or a 3 mM Rudpp concentration in solution, as depicted in Fig. 5. Besides, we did not take into consideration the 20% difference between the Ti-BzAc layer thickness and the height

of derived patterns. All these choices and approximations were sufficient to draw following overall conclusions.

- In all tested conditions, optical modeling shows that a 2.7 μm thick epoxy layer is sufficient to suppress any optical interaction between the substrate and the channel waveguide. In the following parts of this work, the epoxy layer has thus been deposited from a [EETMOS-TEOS] sol concentration of 2 M using a bilayer deposition procedure. The so-obtained cladding layer exhibits a thickness of 3.16 μm and refractive indices at 460 and 610 nm of 1.55 and 1.54, respectively. According to the measured refractive indices of the epoxy and Ti-BzAc layers, the waveguide effective indices were derived from modeling, yielding n_{eff} values of 1.65 and 1.60 at 610 nm and 1.74 and 1.71 at 460 nm for the TE and TM modes, respectively.

- Optical modeling also shows that, for all tested thicknesses and refractive indices, the 2 μm wide waveguide photo-imprinted on this cladding layer is compatible with light propagation at 460 and 610 nm. Owing to its weak thickness, the waveguide is single-mode in the vertical direction, i.e. only the fundamental TE or TM vertical mode can propagate in the waveguide core thickness. Conversely, as the width of the tested waveguide is much greater than the considered wavelengths, the waveguide is multi-mode in the lateral direction, the number of guided modes being larger at the 460 nm wavelength compared to 610 nm. A single-mode channel waveguide would avoid modal interference and would provide a more controlled light pattern in the waveguide, but it would require a width much smaller than 2 μm , which cannot be obtained using our photolithography procedure. In the following parts of this work, we have thus investigated multi-mode waveguides with widths ranging up to 50 μm .

- *Diffraction gratings*

As explained in introduction, the period of diffraction gratings should ideally be of the order of the considered wavelengths (here 460 and 610 nm). As such a period is not accessible with our photolithographic procedure, modelling was performed on a Ti-BzAc grating of 1 μm / 2 μm width / pitch, i.e. the smallest dimensions accessible in this work, photo-imprinted on a Ti-BzAc channel waveguide. We modeled a simplified architecture where light propagating within the waveguide in TE polarization at the 610 nm wavelength is then extracted toward the external medium by coupling with the grating, as schematized in Fig. 2. For this grating, we analyzed patterns of various heights and trapezoidal profiles with a 45° edge slope, and these data were also compared to those derived for patterns with a more ideal square profile, leading to following overall conclusions.

- Compared to what would be obtained with a theoretical infinite grating, optical modeling shows that a grating length of 100 μm , i.e. a grating constituted of 50 periodic patterns, is sufficient to theoretically

diffract around 90% of the light propagating in the waveguide. As illustrated in Fig. 6f, this length is readily achieved in our experimental conditions, and it has been used for further modeling.

- Light is diffracted through the grating according to a finite number of extraction angles, each of them being associated to one given coupling order, as expressed in equation (3). Modeling shows that, in all conditions exposed hereafter, the most efficient light extraction is achieved according to an angle θ_d in the 45-50° range vs the vertical direction, i.e. for $q = 3$ according to equation (3). It is illustrated in Fig. 7 in the case of square and trapezoidal gratings with a 200 nm height.

- A variation of the grating height from 100 to 260 nm only leads to a slight increase of this extraction angle but modeling shows that the most efficient light extraction should be achieved with patterns of 100 nm height (not illustrated here), which has to be compared to the 200-220 nm height obtained in our experimental conditions. A reduction of the pattern height might be achieved through a suitable adaptation of our photolithography procedure, for instance by increasing the post-insolation development duration, or through a reduction in the thickness of the Ti-BzAc layer by using a more diluted sol, but such modifications have not been tested in the present work.

- Finally, optical modeling shows that, compared to theoretical θ_d values derived from the grating law (equation (3)), the simulated values are slightly greater for gratings with square and trapezoidal profiles, this feature being more marked for trapezoidal gratings (Fig. 7). However, for a fixed height, the light extraction efficiency of these latter is rather close to that of square gratings (Fig. 7).

3.4 Channel waveguide / diffraction grating architectures

- *Elaboration and characterization*

Micro-structured architectures were elaborated on the basis of previous experimental features and modeling. A 3.16 μm thick epoxy cladding layer was firstly deposited. A two-step deposition / insolation procedure was then implemented. For simplification purpose, Ti-BzAc layers not doped with Rudpp were studied. In a first step, a Ti-BzAc layer was deposited, heat-treated at 110°C for 10 min and insolated for 40 min through a mask (Fig. 1a). These conditions were fixed in view to obtain channel waveguides of 10 to 50 μm width. In a second step, a new Ti-BzAc layer was deposited, heat-treated at 110°C for 10 min and insolated for 10 min through a mask (Fig. 1b). This latter was designed and positioned to imprint a diffraction grating of 1 μm / 2 μm width / pitch on one selected end of the channel waveguides. The double insolated sample was then heat-treated at 110°C for 8 min, and finally developed in absolute ethanol, rinsed with deionized water and dried with nitrogen spray. Fig. 8 illustrates an example of channel waveguides and diffraction gratings constituting the so-obtained architectures. The optical micrograph of Fig. 8a and the AFM image of Fig. 8b show that long (100 μm or more) and homogeneous diffraction gratings have been selectively imprinted on vicinal waveguides

of uniform width. The gratings exhibit a width/pitch and a height similar to those obtained after a single insolation step, as illustrated in Fig. 6d and f. Fig. 8c depicts an area of a channel waveguide where no grating has been imprinted. Here again, the waveguide exhibits a profile and a height similar to those obtained after a single insolation step, as illustrated in Fig. 6a. Thus, these data globally demonstrate that our two-step deposition / insolation procedure enables to elaborate a channel waveguide / diffraction grating architecture that reliably respects the patterns obtained after a single insolation.

Channel waveguide / diffraction grating coupling was assessed on so-obtained architectures using the optical set-up described in section 2.4. For practical convenience, light at a 610 nm wavelength was injected through a diffraction grating (> 100 μm in length and with a 1 μm / 2 μm width / pitch) at the input of waveguides (1 mm in length and with 10 to 50 μm widths), and it was collected from their polished outlet facet, i.e. a grating – waveguide configuration. This is a reverse configuration compared to the previously modeled one where light was firstly injected in the waveguide and then extracted through the grating, i.e. a waveguide-grating configuration as schematized in Fig. 2. However, owing to the principle of light reciprocity, it was inferred that conclusions drawn from modeling can be extrapolated to the tested configuration. Consequently, light was injected through the grating with an incidence angle of 45°. In this work, we did not use a polarized source and detection was performed without polarization selection. Fig. 9 illustrates the signal emerging from channel waveguides of various widths and the corresponding vertical and horizontal light profiles at the output of a waveguide of 10 μm width. These data depict different guided modes propagating in the waveguide cores and to their interferences (Fig. 9a-c). On the one hand, they confirm that the waveguides are single-mode in the vertical direction (Fig. 9d) even though the spot height is greater than the waveguide thickness owing to light diffraction at the output facet (see broadening at the intensity peak bottom in Fig. 9d). Let us recall that, in this work, the waveguides were imprinted on Ti-BzAc single layers, which yielded a weak waveguide core thickness of 200-220 nm. Thus, only the fundamental (TE or TM) vertical mode can propagate in the thickness of such thin waveguides. On the other hand, the data confirm that the waveguides are multi-mode in the lateral direction and the observed guided modes appear to be distributed on a width that closely matches that of the waveguides (Fig. 9e). All these features provide evidence that the diffraction grating effectively enable light injection in the waveguides and that these allow an efficient guided mode confinement in the vertical and lateral directions. The overall intensity of light emerging from the waveguides was deduced using the MATLAB software. Assessments of waveguides with a width ranging from 10 to 50 μm indicated that the emerging light intensity lay in a rather narrow range of +/- 15%. This observation firstly provides an indication of the reasonable reproducibility in our experimental conditions, even though the XYZ and angle positioning of the

injection fiber has not been optimized. Besides, it enables to conclude that i/ the channel waveguide / diffraction grating coupling efficiency is not significantly influenced by the waveguide width, and ii/ the overall intensity of light propagating in the multi-mode waveguides remains identical regardless of the number of guided modes and their interferences.

- *Architecture assessment: discussion*

The previous data provide a proof of concept that channel waveguide / diffraction grating coupling can effectively be achieved in our sol-gel derived micro-structured architecture. This feature firstly highlights the good concordance between experimental studies and modeling. This concordance is all the more noticeable that modeling has been performed on a waveguide-grating configuration while experiments used the reverse grating-waveguide one. Globally, this work shows that the modeling tools used in this work reliably describe the sol-gel architecture and furnish valuable inputs to guide experimental optimizations, including profile and dimensionality of the components constituting the architecture, as well as angular positioning of the injection fiber used for light coupling through the diffraction grating. Here, channel waveguide / diffraction grating coupling has been assessed in air ($n_{sup} = 1$) at the Rudpp emission wavelength (610 nm). In further investigations, it will be necessary to extrapolate these results to observations in water ($n_{sup} = 1.33$) and at the Rudpp excitation wavelength (460 nm). However, the differences in air and water refractive indices and in the excitation and emission wavelengths being rather small, we can reasonably infer that efficient light coupling is also possible in these new conditions according to suitable experimental adaptation. For instance, the XYZ and angle positioning of the injection fiber will be optimized and, as explained below, the height of trapezoidal diffracting patterns can also be improved in relation to the 460 and 610 nm wavelengths. The present work has been performed using a simplified architecture that involves a diffraction grating positioned at the input of the waveguides. It should be mentioned that such architecture can actually be envisaged for sensor applications in waveguide configuration. For instance, some authors have proposed a sensor where light, injected and extracted through a same diffraction grating positioned at the input of a planar waveguide, undergoes back-reflection on the waveguide output facet [38]. In future stages of our research, we intend to extrapolate our two-step deposition / insolation procedure to the imprinting of diffraction gratings at the input and output of channel waveguides. Before that, since in this work our simplified architecture has led to reliable results, it will be employed in further studies to perform new optimizations. In this simplified architecture, light propagation has also been tested on a rather short length of 1 mm. Several works have shown that such a propagation length is sufficient to propose bio-sensing devices operating in channel waveguide configuration [6, 18]. Of course, our results do not mean that optical losses in Ti-BzAc derived waveguides reduce light propagation to such a short length. Here, we have voluntarily chosen to study short waveguides to draw

first conclusions on our micro-structured sol-gel architecture without being constrained by optical loss problems, and estimation of these losses has been considered to be out of the topics of this preliminary work. Optical losses in our architecture can have different origins, i.e. fiber positioning, grating coupling, light propagation, output facet light extraction... All these features will require optimizations in further studies in order to draw reliable conclusions on these losses. However, the main issue in the next steps of this work addresses Rudpp doping. Indeed, until now only non-doped channel waveguides have been considered since Rudpp does not absorb light at 610 nm and thus cannot modify previous conclusions drawn on waveguide / grating coupling at this wavelength. Conversely, Rudpp absorbs light at the 460 nm excitation wavelength. Consequently, increasing the fluorophore amount in the waveguide should enhance the emission intensity at 610 nm but it should also reduce the excitation light propagation. Rudpp doping relies therefore on a trade-off between both effects and will be optimized in relation to the propagation length on the basis of fluorescence measurements using our simplified architecture. As previously mentioned, the width of multi-mode channel waveguides has no significant effect on the waveguide / grating coupling. Thus, it will be also interesting to study how varying the waveguide width enables to optimize Rudpp doping and propagation length conditions. This optimization of the simplified grating-waveguide architecture will then open the route to first DO sensing assessments in a channel waveguide configuration.

4. Conclusion

This work constitutes a first step toward the development of new chemical optical sensors based on the measurement of Rudpp fluorescence in channel waveguide configuration for the detection of DO. In this context, we intend to propose sol-gel derived micro-structured architectures involving light coupling between channel waveguides and diffraction gratings. Such architectures are expected to enable an enhanced detection sensitivity. This paper particularly highlights the potential of a high refractive index Ti-BzAc sol-gel photoresist that can be imprinted through a single photolithography step (selective insolation / development). Using fluorescence measurements, we have firstly demonstrated that this resist is compatible with Rudpp encapsulation and DO sensing. Then, a simple two-step deposition / insolation sol-gel procedure taking advantage of the Ti-BzAc resist has been developed to imprint a diffraction grating at the input of a channel waveguide. Both components of derived architectures have been studied on the basis of opto-geometrical characterizations and using devoted modeling tools. Then, light coupling between the channel waveguide and the diffraction grating has been assessed. This work notably highlights the good concordance between experimental studies and modeling, showing that the modeling tools used in this work reliably describe the sol-gel

architecture and furnish valuable inputs to guide experimental optimizations, including profile and dimensionality of the components constituting the architecture, as well as angular positioning of the fiber used to inject light through the diffraction grating. According to modeling and experimental optimizations, trapezoidal diffraction gratings (200-220 nm height, 1 μm / 2 μm width / pitch, 45° edge slope and a length of 100 μm or more) have been imprinted on channel waveguides (10 to 50 μm width and 1 mm length), and we have demonstrated that derived architectures are compatible with waveguide / grating coupling. To our best knowledge, such coupling has never been reported before using a sol-gel derived architecture. Several optimization ways can now be envisaged to enhance again this coupling and light propagation in the waveguide core. In a next step of this work, it will be particularly necessary to tailor the amount of encapsulated Rudpp in relation to the waveguide width and length in order to optimize the light propagation and the fluorescence intensity. This optimization will open the route to first DO sensing assessments in channel waveguide configuration.

Acknowledgements: The authors thank the Labex CEMAM and the Grenoble Alpes University for financial supports.

References

- [1] C. Demuth, J. Varonier, V. Jossen, R. Eibl, D. Eibl, Novel probes for pH and dissolved oxygen measurements in cultivations from millilitre to benchtop scale, *Appl Microbiol Biotechnol* 100 (2016) 3853.
- [2] M. Barczak, C. McDonagh, D. Wencel, Micro- and nanostructured sol-gel based materials for optical chemical sensing, *Microchim Acta* 183 (2016) 2085.
- [3] B. Kuswandi, Nuriman, J. Huskens, W. Verboom, Optical sensing systems for microfluidic devices: a review, *Anal Chim Acta* 601 (2007) 141.
- [4] H. Mukundan, A.S. Anderson, W.K. Grace, K.M. Grace, N. Hartman, J.S. Martinez, B.I. Swanson, Waveguide-based biosensors for pathogen detection, *Sensors* 9 (2009) 5783.
- [5] P.V. Lambeck, Integrated optical sensors for the chemical domain, *Meas Sci Technol* 17 (2006) R93.
- [6] M.D. Stephens, G. Yuan, K.L. Lear, D.S. Dandy, Optical and physical characterization of a local evanescent array coupled biosensor: use of evanescent field perturbations for multianalyte sensing, *Sens Actuators B* 145 (2010) 769.
- [7] T. Mayr, T. Abel, B. Enko, S. Borisov, C. Konrad, S. Köstler, B. Lamprecht, S. Sax, E.J.W. List, I. Klimant, A planar waveguide optical sensor employing simple light coupling, *Anal* 134 (2009) 1544.

- [8] D.S. Bagal, A. Vijayan, R.C. Aiyer, R.N. Karekar, M.S. Karve, Fabrication of sucrose biosensor based on single mode planar optical waveguide using co-immobilized plant invertase and GOD, *Biosens Bioelectron* 22 (2007) 3072.
- [9] X. Xing, W. Liu, T. Li, S. Xing, X. Fu, D. Wu, D. Liu, Z. Wang, A portable optical waveguide resonance light-scattering scanner for microarray detection, *Anal* 141 (2016) 199.
- [10] R. Yan, S.P. Mestas, G. Yuan, D.S. Dandy, K.L. Lear, Label-free silicon photonic biosensor system with integrated detector array, *Lab Chip* 9 (2009) 2163.
- [11] R. Yan, N.S. Lynn, L.C. Kingry, Z. Yi, R.A. Slayden, D.S. Dandy, K.L. Lear, Waveguide biosensor with integrated detector array for tuberculosis testing, *Appl Phys Lett* 98 (2011) 013702.
- [12] R.J. Ram, K. Lee, Optical waveguides for microfluidic integration, *LEOS Ann Meet Conf Proc*, 2009.
- [13] E. Benito-Pena, M. Granda Valdes, B. Glahn-Martinez, M.C. Moreno-Bondi, Fluorescence based fiber and planar waveguide biosensors: a review, *Anal Chim Acta* 943 (2016) 17.
- [14] C.S. Burke, L. Polerecky, B.D. MacCraith, Design and fabrication of enhanced polymer waveguide platforms for absorption-based optical chemical sensors, *Meas Sci Technol* 15 (2004) 1140.
- [15] M. Hajj-Hassan, T. Gonzalez, E. Ghafar-Zadeh, H. Djeghelian, V. Chodavarapu, M. Andrews, D. Therriault, Direct-dispense polymeric waveguides platform for optical chemical sensors, *Sens* 8 (2008) 7636.
- [16] M. Bedu, G. Sagarzazu, T. Gacoin, P. Audebert, C. Weisbuch, L. Martinelli, Sol-gel planar waveguides for improved fluorescence microarrays, *Thin Solid Films* 518 (2010) 4450.
- [17] R. Copperwhite, M. O'Sullivan, C. Boothman, A. Gorin, C. McDonagh, M. Oubaha, Development and characterisation of integrated microfluidics on waveguide-based platforms fabricated from hybrid materials, *Microfluid Nanofluid* 11 (2011) 283.
- [18] M. Oubaha, A. Gorin, C. McDonagh, B. Duffy, R. Copperwhite, Development of a multianalyte optical sol-gel biosensor for medical diagnostic, *Sens Actuators B* 221 (2015) 96.
- [19] Y. Enami, T. Fukuda, S. Suye, Sol-gel silica planar waveguide doped with green luminescent protein for in-line biosensors, *Appl Phys Lett* 91 (2007) 203507.
- [20] S.D. Le, E. Delcourt, P. Girault, A. Gutierrez-Arroyo, P. Azuelos, N. Lorrain, L. Bodiou, L. Poffo, J.M. Goujon, Y. Dumeige, I. Hardy, P. Rochard, J. Lemaitre, P. Pirasteh, M. Guendouz, T. Chartier, L. Quétel, S. Claudot, J. Charrier, M. Thual, Study of optimized coupling based on micro-lensed fibers for fibers and photonic integrated circuits in the framework of telecommunication and sensing applications, *Comm Phys* 26 (2016) 325.
- [21] D. Dai, Y. Tang, J.E. Bowers, Mode conversion in tapered submicron silicon ridge optical waveguides, *Opt Exp* 20 (2012) 13425.

- [22] J. Cardenas, C.B. Poitras, K. Luke, L.W. Luo, P.A. Morton, M. Lipson, High coupling efficiency etched facet tapers in silicon waveguides, *IEEE Photon Technol Lett* 26 (2014) 2380.
- [23] J. Liu, A.S. Raja, M.H.P. Pfeiffer, C. Herkommer, H. Guo, M. Zervas, M. Geiselmann, T. Kippenberg, Double inverse nanotapers for efficient light coupling to integrated photonic devices, *Opt. Lett.* 43 (2018) 3200.
- [24] D. Taillaert, F. Van Laere, M. Ayre, W. Bogaerts, D. Van Thourhout, P. Bienstman, R. Baets, Grating couplers for coupling between optical fibers, *Jpn J Appl Phys* 45 (2006) 6071.
- [25] S. Briche, D. Riassetto, C. Gastaldin, C. Lamarle, O. Dellea, D. Jamon, E. Pernot, M. Labeau, G. Ravel, M. Langlet, Sol-Gel processing and UVA patterning of epoxy-based hybrid organic-inorganic thin films, *J Mater Sci* 43 (2008) 5809.
- [26] S. Briche, Z. Tebby, D. Riassetto, M. Messaoud, E. Gamet, E. Pernot, H. Roussel, O. Dellea, Y. Jourlin, M. Langlet, New insights in photo-patterned sol-gel derived TiO₂ films, *J Mater Sci* 46 (2011) 1474.
- [27] H. Kogelnik, V. Ramaswamy, Scaling rules for thin-film optical waveguides, *Appl Opt* 13 (1974) 1857.
- [28] B.E.A. Saleh, M.C. Teich, *Fundamental of photonics*, 2nd ed., Wiley, 2007, p. 304.
- [29] A. Yariv, P. Yeh, *Photonics: optical electronic in modern communications*, Oxford University Press, New York, 2006, p. 580.
- [30] J.P. Hugonin, P. Lalanne, Perfectly matched layers as nonlinear coordinate transforms: a generalized formalization, *J Opt Soc Am A* 22 (2005) 1844.
- [31] D. Bucci, B. Martin, A. Morand, Application of the three-dimensional aperiodic Fourier modal method using arc elements in curvilinear coordinates, *J Opt Soc Am A* 29 (2012) 367.
- [32] G.A. Baker, B.R. Wenner, A.N. Watkins, F.V. Bright, Effects of processing temperature on the oxygen quenching behaviour of tris(4,7'-diphenyl-1,10'-phenanthroline) Ruthenium (II) sequestered within sol-gel-derived xerogels films, *J Sol-Gel Sci Technol* 17 (2000) 71.
- [33] C.W. Chang, C.K. Chou, I.J. Chang, Y.P. Lee, E.W.G. Diau, Relaxation dynamics of ruthenium complexes in solution, PMMA and TiO₂ films: the roles of self-quenching and interfacial electron transfer, *J Phys Chem C* 111 (2007) 13288.
- [34] A. Mills, A. Graham, C. O'Rourke, A novel titania sol-gel derived film for luminescence-based oxygen sensing, *Sens Actuators B* 190 (2014) 907.
- [35] J.R. Lakowicz, *Principles of fluorescence spectroscopy*, 2nd ed., Kluwer Academic/Plenum Publishers, New York, 1999, p. 54.
- [36] V. Gâté, Y. Jourlin, F. Vocanson, O. Dellea, G. Vercasson, S. Reynaud, D. Riassetto, M. Langlet, Sub-micrometric patterns written using a DIL method coupled to a TiO₂ photo-resist, *Opt Mater* 35 (2013) 1706.

- [37] O. Shavdina, L. Berthod, T. Kämpfe, S. Reynaud, C. Veillas, I. Verrier, M. Langlet, F. Vocanson, P. Fugier, Y. Jourlin, O. Dellea, Large area fabrication of periodic TiO₂ nanopillars using microsphere photolithography on a photopatternable sol-gel film, *Langmuir* 31 (2015) 7877.
- [38] A. Demeter, S. Ruschin, Back-reflecting interferometric sensor based on grating coupler on a planar waveguide, *J Opt* 18 (2016) 015801.

Figure captions

Fig. 1. Schematic flow diagram of the two-step deposition / insolation procedure leading to the photo-imprinting of a channel waveguide (a) followed by that of a diffraction grating (b). The parentheses correspond to optional steps. In b, the view has been rotated by 90° in the horizontal plane.

Fig. 2. Schematic view of the channel waveguide / diffraction grating architecture considered for modeling. The signification of the letters is explained in the text.

Fig. 3. Fluorescence emission intensity at 610 nm measured under excitation at 460 nm in water (a) and in air (b) for a Rudpp-doped Ti-BzAc layer. The inset shows corresponding emission spectra.

Fig. 4. Left: Epoxy layer thickness variations as a function of the number of single layers for a sol of 1.5 M [EETMOS-TEOS] concentration (a) and as a function of the [EETMOS-TEOS] concentration for one single layer (b); Right: Variations of the epoxy layer refractive index at 460 nm (a) and 610 nm (b) as a function of the number of single layers for a sol of 1.5 M [EETMOS-TEOS] concentration.

Fig. 5. Influence of the Rudpp concentration in solution on the thickness and on the refractive index at 460 nm (a) and 610 nm (b) for Rudpp-doped Ti-BzAc layers.

Fig. 6. Illustration of Ti-BzAc patterns photo-imprinted using the first step of the experimental procedure illustrated in Fig 1a: AFM images for patterns with 5 μm spacing and 10 μm width (a) and patterns of 1 μm / 2 μm width / pitch (b); profilometry data for a 50 μm wide pattern (c) and for patterns of 4 μm / 8 μm width / pitch (d); optical micrographs of a 50 μm wide pattern (e) and patterns of 1 μm / 2 μm width / pitch (f). In f, the inset illustrates a Ti-BzAc layer area not photo-patterned (left) and an area photo-patterned using a mask with transparent strips of 1 μm / 2 μm width / pitch (right).

Fig. 7. Intensity profile of light ($\lambda = 610$ nm) extracted from a channel waveguide through a diffraction grating of 1 μm / 2 μm width / pitch, according to the configuration illustrated in Fig. 2, for 200 nm height gratings with a square (dotted blue lines) and a trapezoidal profile (full black lines). The light intensity has been normalized according to the maximal value obtained in the case of a square profile for a diffraction angle θ_d around 45°. The red lines depict the theoretical diffraction angles deduced from the grating law (equation (3)).

Fig. 8. Illustration of Ti-BzAc patterns photo-imprinted using the whole experimental procedure illustrated in Fig 1: optical micrograph (a) and AFM image (b) for a diffraction grating of 1 μm / 2 μm

width / pitch photo-imprinted on the top of vicinal channel waveguides and profilometry data for a channel waveguide in an area where no grating has been imprinted (c).

Fig. 9. Illustration of the signal emerging from waveguides of 1 mm length and widths of 10 μm (a), 20 μm (b) and 50 μm (c) after light injection through a diffraction grating (the scale bar is the same for all the pictures), and corresponding vertical (d) and horizontal intensity profiles (e) in the light propagation direction for a waveguide of 10 μm width.

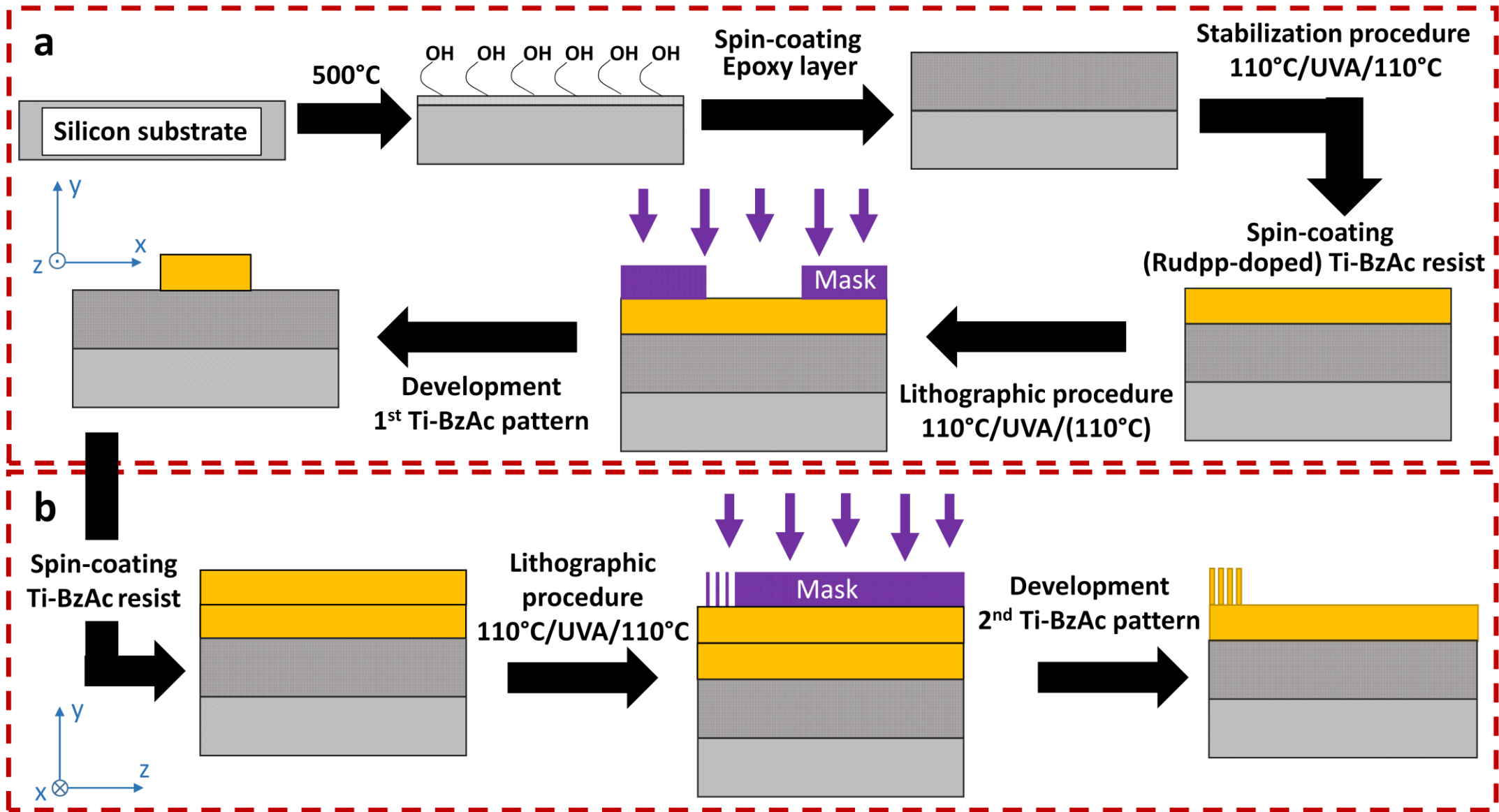


Fig. 1. Schematic flow diagram of the two-step deposition / insulation procedure leading to the photo-imprinting of a channel waveguide (a) followed by that of a diffraction grating (b). The parentheses correspond to optional steps. In b, the view has been rotated by 90° in the horizontal plane.

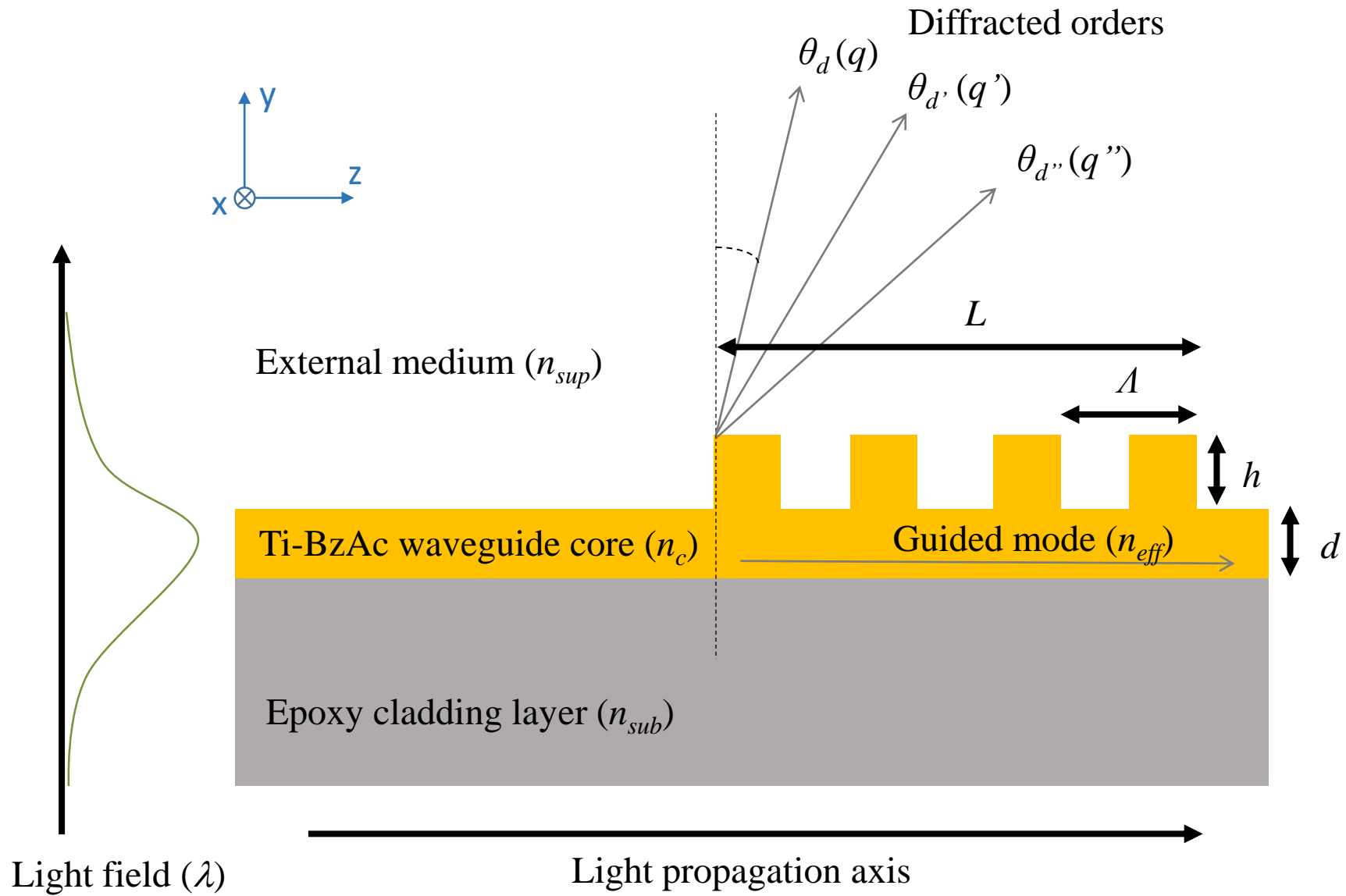


Fig. 2. Schematic view of the channel waveguide / diffraction grating architecture considered for modeling. The signification of the letters is explained in the text.

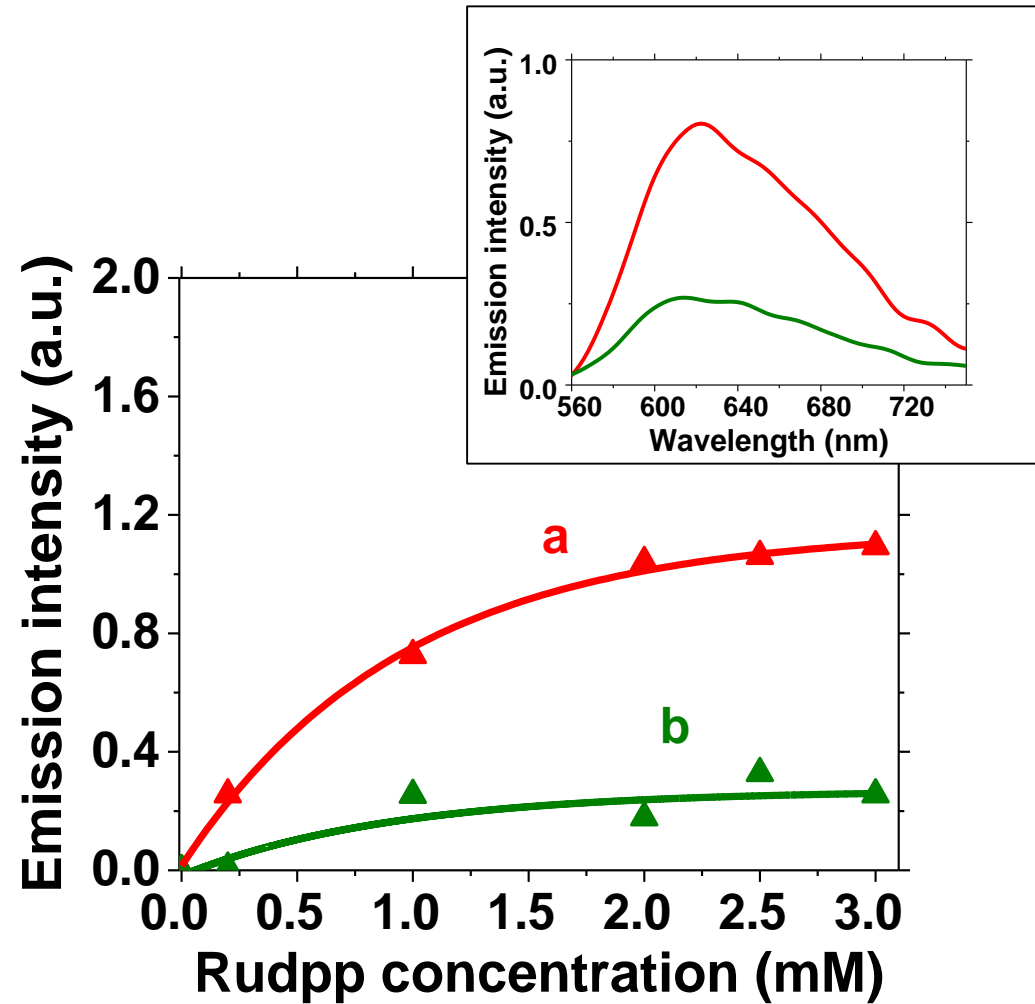


Fig. 3. Fluorescence emission intensity at 610 nm measured under excitation at 460 nm in water (a) and in air (b) for a Rudpp-doped Ti-BzAc layer. The inset shows corresponding emission spectra.

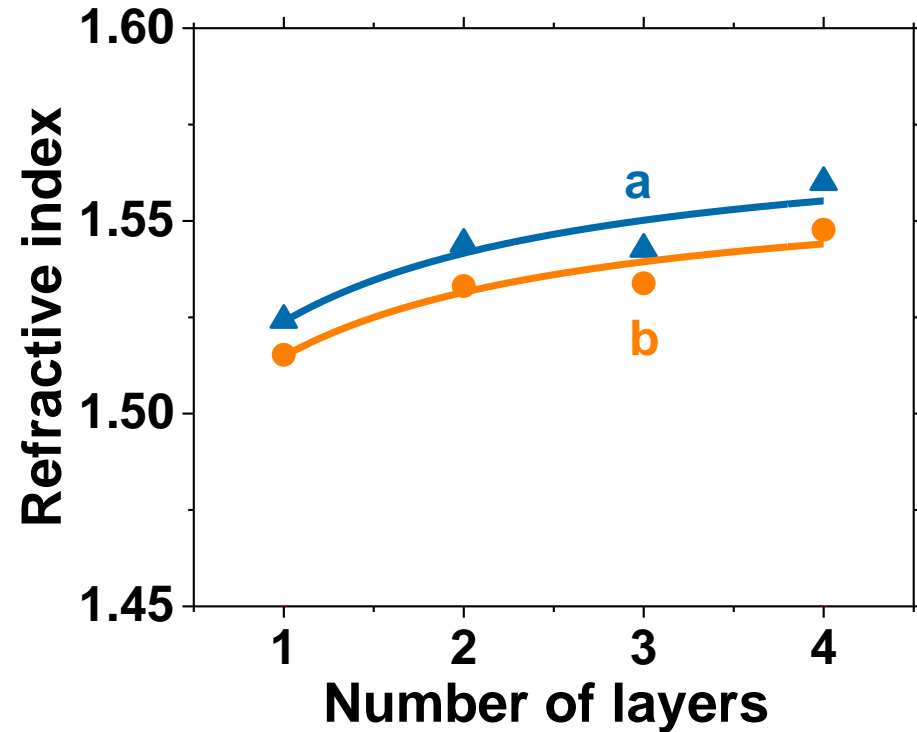
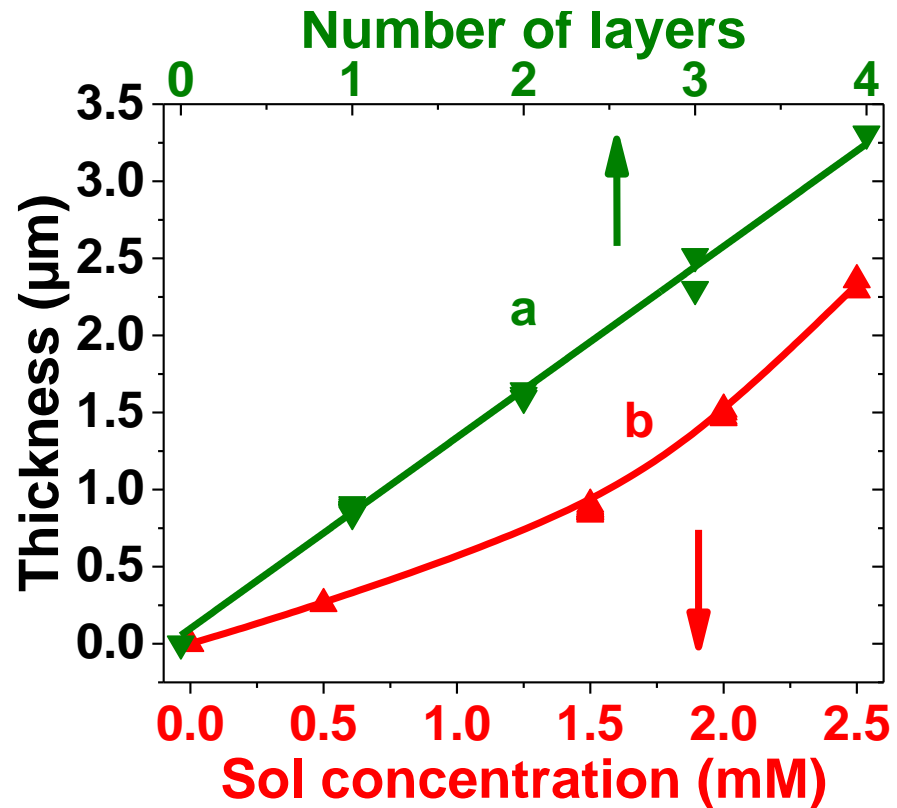


Fig. 4. Left: Epoxy layer thickness variations as a function of the number of single layers for a sol of 1.5 M [EETMOS-TEOS] concentration (a) and as a function of the [EETMOS-TEOS] concentration for one single layer (b); Right: Variations of the epoxy layer refractive index at 460 nm (a) and 610 nm (b) as a function of the number of single layers for a sol of 1.5 M [EETMOS-TEOS] concentration.

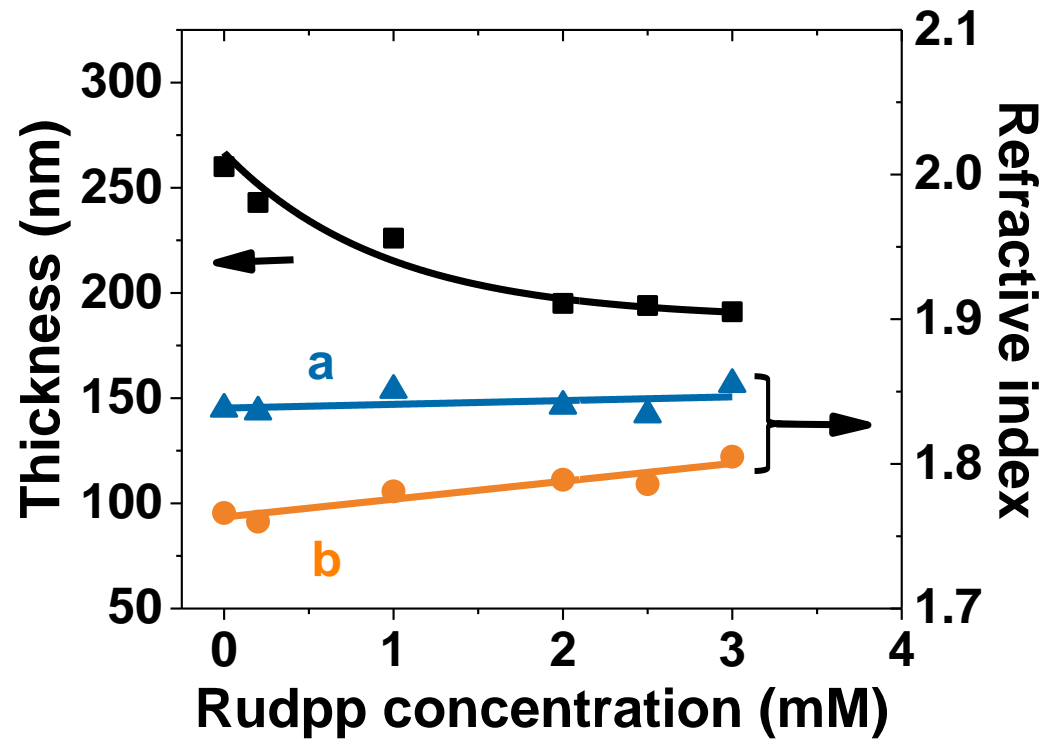


Fig. 5. Influence of the Rudpp concentration in solution on the thickness and on the refractive index at 460 nm (a) and 610 nm (b) for Rudpp-doped Ti-BzAc layers.

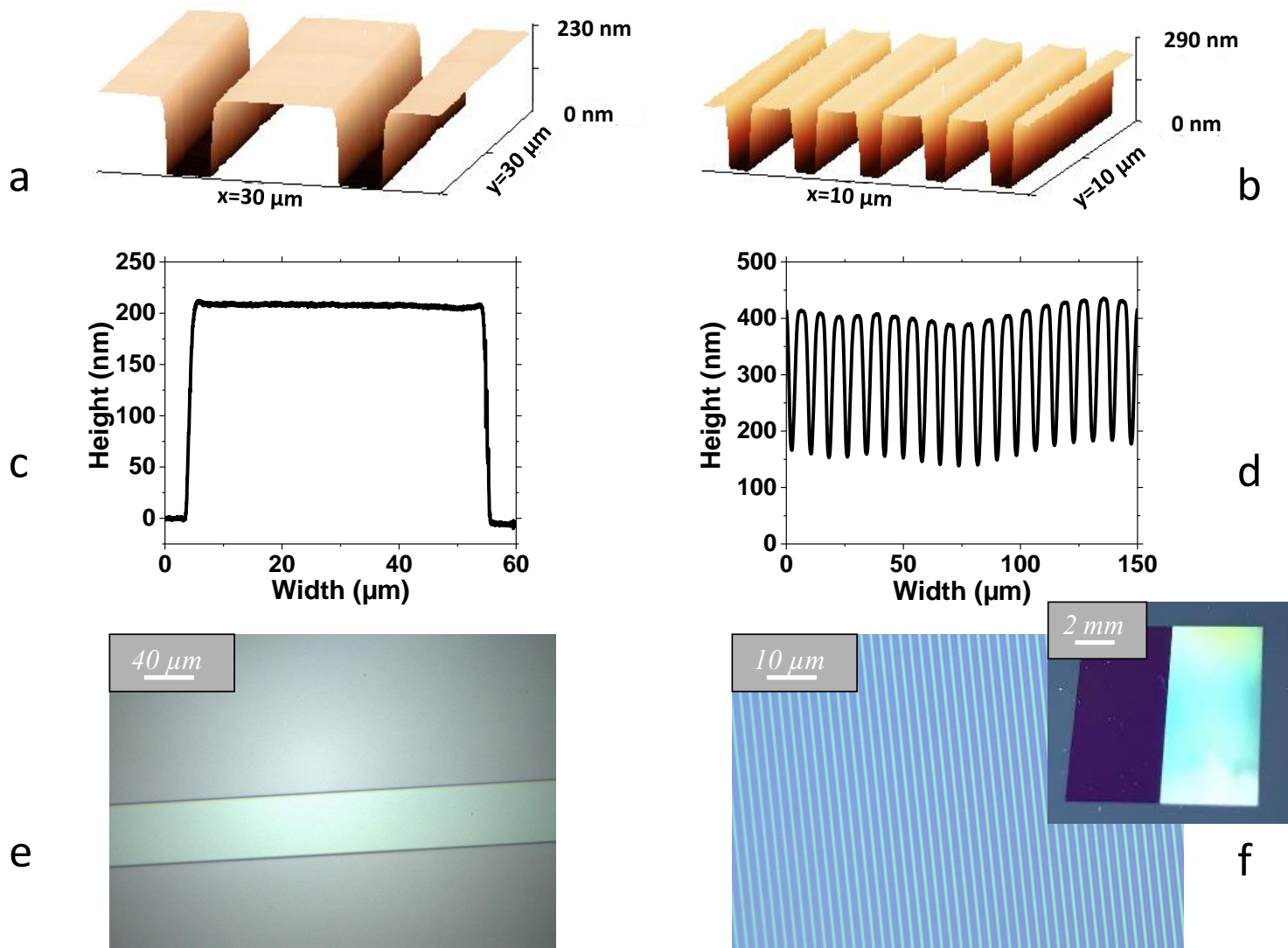


Fig. 6. Illustration of Ti-BzAc patterns photo-imprinted using the first step of the experimental procedure illustrated in Fig 1a: AFM images for patterns with 5 μm spacing and 10 μm width (a) and patterns of 1 μm / 2 μm width / pitch (b); profilometry data for a 50 μm wide pattern (c) and for patterns of 4 μm / 8 μm width / pitch (d); optical micrographs of a 50 μm wide pattern (e) and patterns of 1 μm / 2 μm width / pitch (f). In f, the inset illustrates a Ti-BzAc layer area not photo-patterned (left) and an area photo-patterned using a mask with transparent strips of 1 μm / 2 μm width / pitch (right).

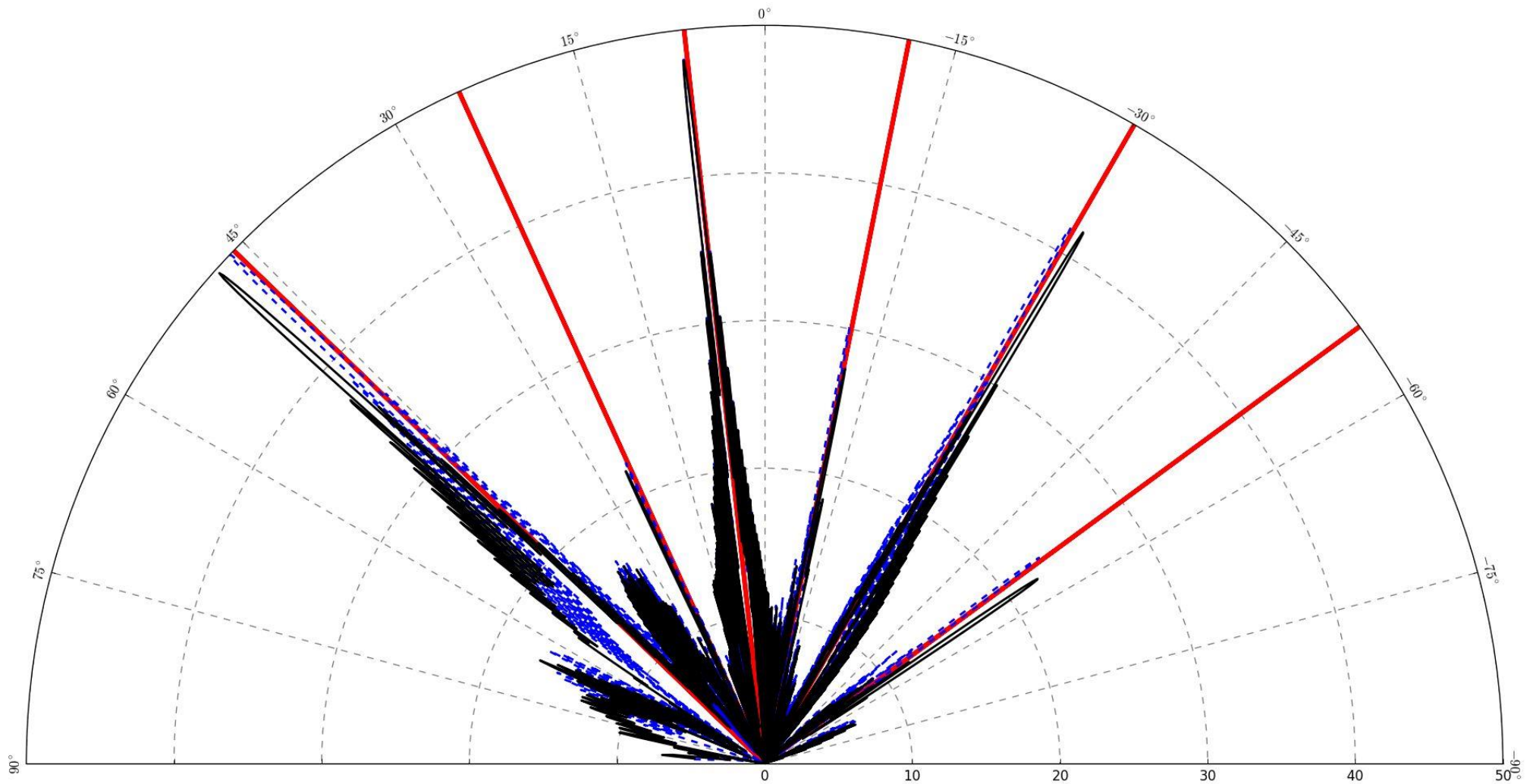


Fig. 7. Intensity profile of light ($\lambda = 610$ nm) extracted from a channel waveguide through a diffraction grating of $1 \mu\text{m} / 2 \mu\text{m}$ width / pitch, according to the configuration illustrated in Fig. 2, for 200 nm height gratings with a square (dotted blue lines) and a trapezoidal profile (full black lines). The light intensity has been normalized according to the maximal value obtained in the case of a square profile for a diffraction angle θ_d around 45° . The red lines depict the theoretical diffraction angles deduced from the grating law (equation (3)).

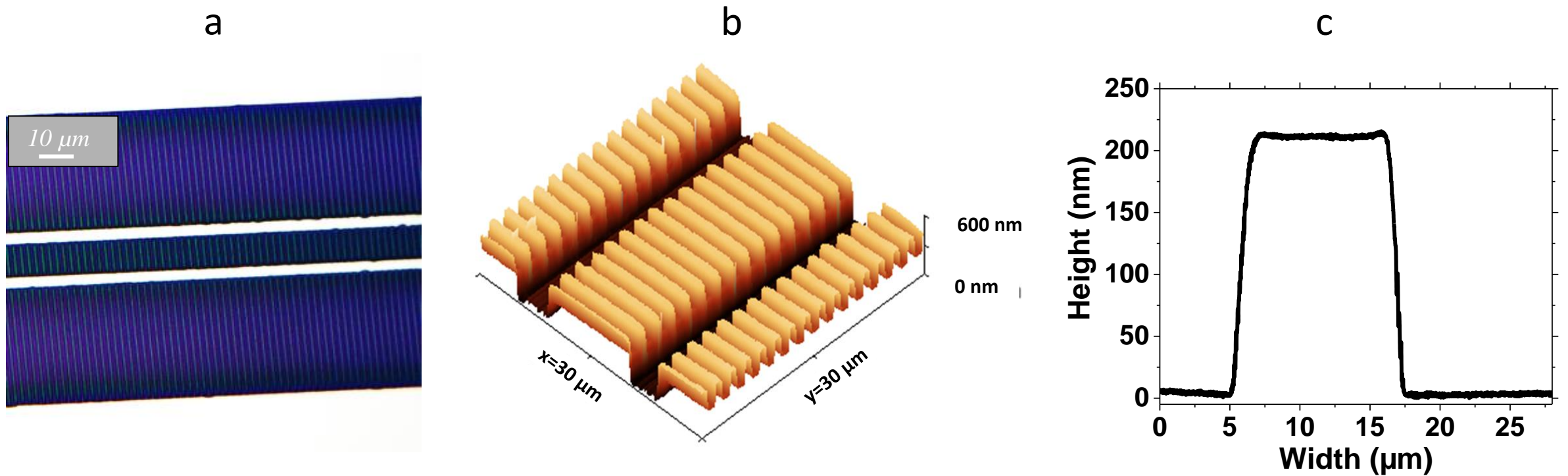


Fig. 8. Illustration of Ti-BzAc patterns photo-imprinted using the whole experimental procedure illustrated in Fig 1: optical micrograph (a) and AFM image (b) for a diffraction grating of $1\ \mu\text{m} / 2\ \mu\text{m}$ width / pitch photo-imprinted on the top of vicinal channel waveguides and profilometry data for a channel waveguide in an area where no grating has been imprinted (c).

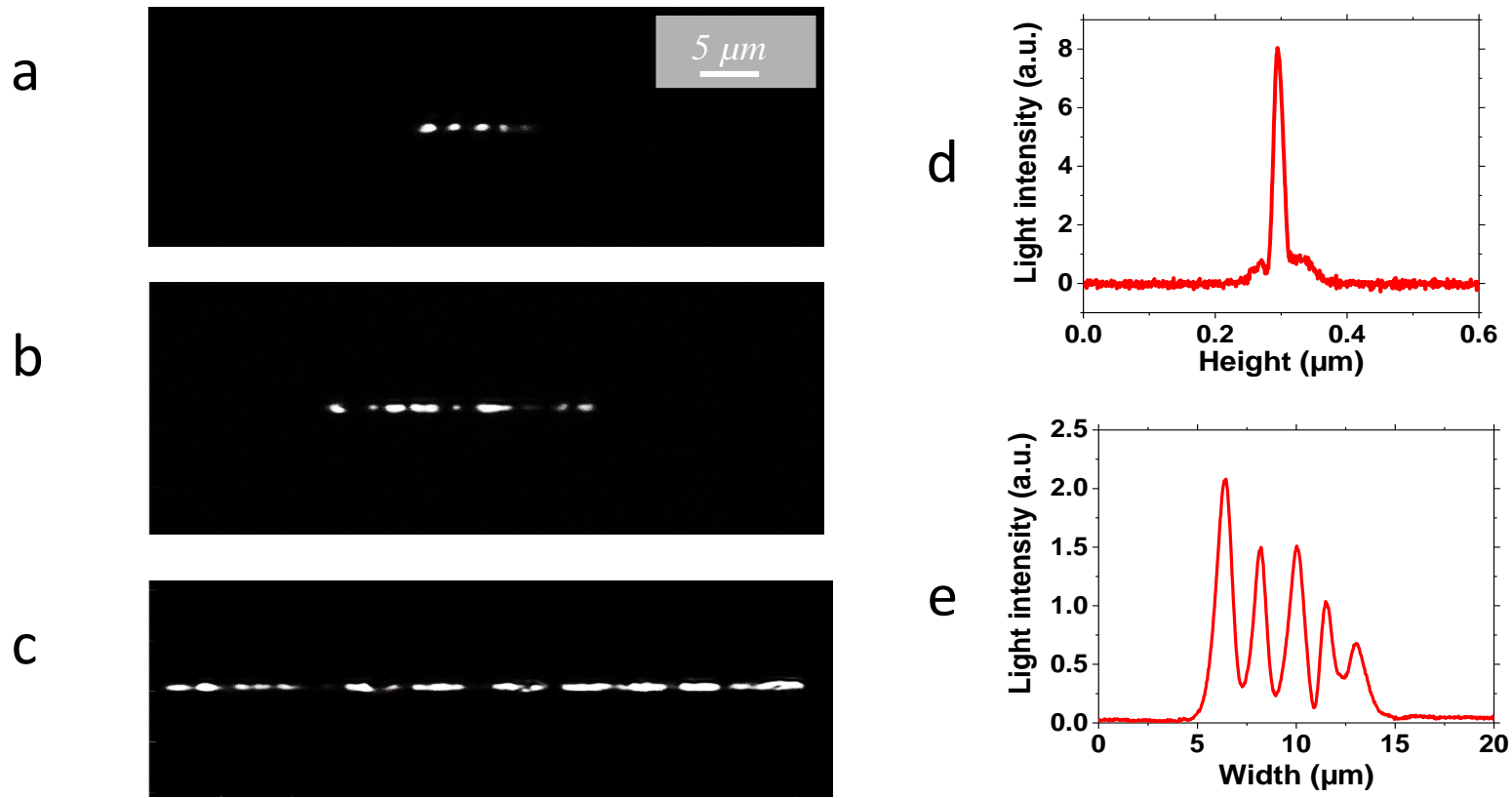


Fig. 9. Illustration of the signal emerging from waveguides of 1 mm length and widths of 10 μm (a), 20 μm (b) and 50 μm (c) after light injection through a 1 μm / 2 μm width / pitch diffraction grating (the scale bar is the same for all the pictures), and corresponding vertical (d) and horizontal intensity profiles (e) in the propagation direction for a waveguide of 10 μm width.